



# A Unified Algorithm for the Young–Laplace Method Applied to Porous Media

Alexandre Miers Zobot<sup>1</sup>  · Mario Augusto Camargo<sup>2</sup>  · Fabiano Gilberto Wolf<sup>3</sup>  · Diogo Nardelli Siebert<sup>1</sup>  · Rodrigo Surmas<sup>4</sup>  · Luis Orlando Emerich dos Santos<sup>1</sup>  · Talita Rosas Ferreira<sup>5</sup>  · Fábio Augusto Meira Cássaro<sup>6</sup>  · Luiz Fernando Pires<sup>6</sup> 

Received: 8 November 2022 / Accepted: 16 February 2024 / Published online: 24 February 2024  
© The Author(s) under exclusive licence to Sociedade Brasileira de Física 2024

## Abstract

Young–Laplace equation-based algorithms for simulating capillary-driven flow have been used in porous media research for more than two decades. However, the lack of a uniform mathematical description hinders a wider application of these algorithms, as well as impede their comparison. After conducting a detailed review of the most important publications in the area, we propose a unified algorithm. This resulting framework is capable of handling four distinct physical situations: drainage and imbibition with either compressible or incompressible displacement fluid. Additionally, there is no restriction regarding the geometry or the initial fluid distribution used. The proposed algorithm can simulate variable or mixed wettability, even for imbibition, which has not already been described in the literature. Finally, at the end of the manuscript, we provide an efficient open-source C++ code for the proposed unified algorithm and also many examples of its use.

**Keywords** Two-phase fluid flow · Contact angle · Drainage · Imbibition · Mathematical morphology · Capillary pressure curve

## 1 Introduction

The numerical method discussed in this work has received different names in the literature throughout the years. Names such as Full Morphology [1, 2], Pore-morphology-based

Simulation [3–6], Pore Morphology [7, 8], Morphological [9] Approach, and Capillary Drainage Transform [10, 11] are found in the literature for Young–Laplace equation-based algorithms. Hereafter, the technique will be referred to as the Young–Laplace Method (YLM). This choice intends to clearly state the physical principle behind the method, which is related to the Young–Laplace equation (Eq. (1)), which fundamentally computes capillary forces that are involved in capillary-driven displacements.

The YLM was independently proposed in the late 1990s and initial 2000s by Hazlett [12], Magnani [13], and Magnani et al. [14]. Nonetheless, most of the cited literature in the area recognized Hazlett [12] as the sole creator of the method. Based on the hypothesis that the fluid invasion in a porous medium is exclusively limited by the capillary pressure, they proposed a sequence of steps to simulate both imbibition and drainage processes, even if no name was given to this new method. The YLM is capable of determining the spatial distribution of two immiscible fluids inside any porous geometry for a value of capillary pressure. This result is obtained under the assumption that the fluid distribution only depends on the mechanical equilibrium between the applied pressure difference and capillary forces. With this approach, dynamic effects are neglected and the fluid invasion is thought of as being a

✉ Mario Augusto Camargo  
mario.camargo@ifsc.edu.br

<sup>1</sup> Porous Media Research Group (PORO), Scientific Computational Laboratory, Federal University of Santa Catarina, 89219-600 Joinville, SC, Brazil

<sup>2</sup> Federal Institute of Santa Catarina (IFSC), 89466-312 Canoinhas, SC, Brazil

<sup>3</sup> Porous Media Research Group (PORO), Microfluidics Laboratory, Federal University of Santa Catarina, 89219-600 Joinville, SC, Brazil

<sup>4</sup> Leopoldo Américo Miguez de Mello Research and Development Center (CENPES/Petrobras), 21941-598 Rio de Janeiro, RJ, Brazil

<sup>5</sup> National Synchrotron Light Laboratory (LNLS), Brazilian Center for Research in Energy and Materials (CNPEM), 13083-100 Campinas, SP, Brazil

<sup>6</sup> Laboratory of Physics Applied To Soils and Environmental Sciences (FASCA), State University of Ponta Grossa (UEPG), 84.030-900 Ponta Grossa, PR, Brazil

quasi-static process. This is a strong hypothesis that allows for a very efficient computational method and has a great impact on the practical applicability of the technique.

Despite the applicability limitations, a renewed interest in the method has emerged in recent years. This can be attested by the fact that more than ever, manuscripts applying YLM were published in these past years. A possible reason for this greater interest is the expansion in access to 3D imaging tools (e.g., 3D microtomography ( $\mu$ CT)) and also in the acquisition of physical properties by image analysis, for example, in digital petrophysics. Since the method makes no assumption regarding the geometry and it has a low computational cost, it is an excellent tool for the first analysis of digital rock images.

Most of the important applications were published only 10 years after the method was created when the use of digital rock images obtained by  $\mu$ CT started to gain popularity. Vogel et al. [2] compared the use of YLM, Lattice–Boltzmann Method (LBM), and Pore Network Modeling (PNM) to compute the capillary curve. The authors used  $\mu$ CT images of a borosilicate cylinder with a size of  $98^3$  voxels. It was found that the computational cost of the YLM was similar to the PNM, which in turn was thousands of times lower than that of LBM. It is important to emphasize that both the LBM and the PNM can determine transport properties of the flow like permeability, whereas as said, the YLM is limited to the quasi-static circumstances. Regarding the capillary curve, all mentioned methods showed equivalent results. Schulz et al. [1] applied the YLM to study the gas diffusion layer inside a polymer electrolyte fuel cell as the presence of water in reaction sites hinders the efficiency of the cell. Shikhov and Arns [6] employed the YLM to simulate three capillary pressure experiments: Porous Plate, Centrifuge Multi-speed, and Mercury Intrusion Porosimetry. Obtained results revealed that heterogeneities play a significant role in the experimental results, and they concluded that the numerical simulations using YLM can help to better delineate laboratory experiments.

The determination of relative permeability employing the YLM is another interesting application that emerged in recent years [7, 9, 15, 16]. Although limited to quasi-static phenomena, the method is combined with dynamical methods to assess this property. In this approach, the YLM computes the space distribution of the fluids in an interest capillary pressure then the distribution is used as input data in a dynamical method (like LBM) to determine the flow rate in the percolating phase.

The lack of a proper and uniform name is a minor difficulty one will face trying to apply the YLM. A greater obstacle is the absence of detailed information regarding its implementation. Except for a few papers [4, 14], most

works are restricted to describing the general characteristics of the method, even when relevant changes are proposed [9]. Frequently, critical computational aspects that can impact computational efficiency are not properly discussed. This prevents the comparison of obtained results with different implementations, difficult to replicate computational simulations for improving the algorithm, and makes unclear whether new developments affect computational efficiency.

In this paper, we present a unified algorithm for the Young–Laplace Method where both drainage and imbibition processes are considered in a single framework. It incorporates several existing improvements for drainage simulation [4, 5], and it correctly describes the presence of ganglia (quantities of fluid entrapped in the pore space, like bubbles). A more detailed description of the improvements implemented in the works of Hilpert and Miller [4] and Schutz et al. [5] is done in Appendix 2. More than just a grouping of previous works, we propose a new and coherent mathematical formalism that simplifies the understanding of the method and sets the basis upon which new improvements can be proposed. Moreover, an efficient C++ code using this new structure is made available using the GNU GPLv3 software.

The paper is organized as follows. In Sect. 2, we describe some basic physical concepts regarding YLM. Section 3 presents our unified algorithm for the YLM and its formal mathematical description using the notation of set operations. In Sect. 4, we discuss the YLM for the imbibition case, which, so far, is not a well-addressed question. We show that the correction from Hilpert and Miller [4] does not need to be applied in this case and also reveal how to apply Schulz et al.'s [5] variable contact angles for imbibition processes. Finally, Sect. 5 summarizes the conclusions of the paper.

## 2 Basic Concepts

The main purpose of the YLM is to find the spatial distribution of both the invading and displaced fluid inside a porous media, without employing dynamical equations. Since it is limited to the prediction of the equilibrium states of capillary pressure under this condition, it is commonly regarded as a quasi-static method.

YLM relies on the Young–Laplace equation to determine the interface liquid curvature in the non-wetting and wetting phases [17]. Additionally, the method employs an approximation that the two radii of curvature ( $R$ ) are equal which, for a cylindrical capillary tube results on

$$P_c = P_N - P_W = \frac{2\sigma \cos\theta}{r_c} \quad (1)$$

where  $P_c$  is the capillary pressure, i.e., the difference between the pressure in the non-wetting ( $P_N$ ) and wetting ( $P_W$ ) phases, and  $\sigma$  is the interfacial tension. As shown in Fig. 1a,  $\theta$  is the wetting fluid contact angle, and  $r_c$  is the capillary radius ( $r_c = R \cos \theta$ ).

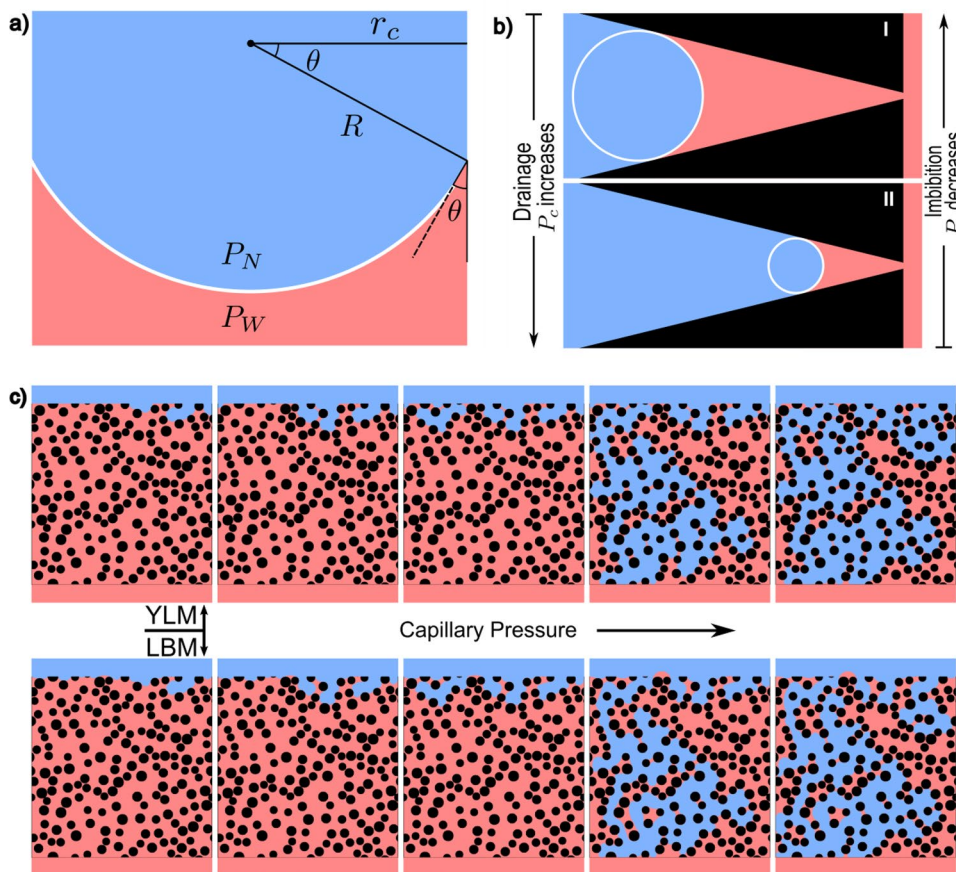
As seen in Eq. (1), the importance of capillary pressure in multiphase fluid flows is evident as the capillary radius decreases, especially in strongly wetting conditions. Therefore, modeling multiphase flows in porous media needs to consider the influence of capillary effects, as both the fluid flow dynamics in micro- and nanopores and the thermodynamic properties of the phases involved can be altered [18–21]. Figure 1b shows how the regions occupied by each fluid are affected by the change in capillary or applied pressure for a capillary tube with a variable cross-section. In the upper section, the non-wetting fluid (blue) cannot access the narrower part of the channel because a low-pressure value corresponds to a large curvature radius. In the narrower section, the pressure difference is increased, and the new equilibrium is related to smaller radii. The main idea behind the YLM, as proposed by Hazlett [12] and Magnani [13] came from a simple idea. Considering a null contact angle and a given value of  $P_c$ , a region can only be occupied by the non-wetting fluid if it is possible to inscribe a sphere of radius  $R = 2\sigma/P_c$  inside this region.

Figure 1b presents scenarios where the two fluids are statically in equilibrium. In the absence of fluid motion, the two fluids should remain in this configuration. If a dynamic process of invasion is carried out with a low capillary number (when capillary forces are dominant over the viscous ones), then we expect the system to pass through these configurations during the invasion process. Thus, finding these states is also necessary for understanding dynamic processes.

During drainage, increasing the pressure associated with the injected non-wetting fluid displaces the wetting fluid that initially fills the porous media. The increase occurs in small steps to allow the fluids to reach new equilibrium configurations. On the other hand, imbibition happens when the wetting fluid invades the region previously filled by the non-wetting fluid when the pressure of the latter is decreased. Using Fig. 1b as an illustration, during the drainage the system would go from states I to II, whereas for the imbibition, the wetting front evolution is the opposite.

Figure 1c shows a comparison between the equilibrium states of drainage predicted by the YLM and by the Shan–Chen multicomponent LBM (SC-LBM) [22–25]. Despite some small differences, the results from the YLM are pretty close to the ones from SC-LBM, showing that the method can predict the static equilibrium states of this stepwise invasion process.

**Fig. 1** The non-wetting and wetting fluids are presented in blue and red, respectively. **a** Capillary rise of a wetting fluid in a cylindrical tube. The figure depicts the longitudinal section of the tube. **b** Two equilibrium states for different values of the capillary pressure ( $P_c$ ).  $P_c^{(I)} < P_c^{(II)}$ , resulting in a larger curvature radius in the upper case. **c** Comparison between equilibrium states obtained by YLM and LBM for a drainage process



In this study, we included the results of SC-LBM simulations as an indication of quality to show that YLM provides satisfactory results for the invasion process. Although we considered an idealized porous medium, the LBM (and its variations) has been considered a very powerful tool for predicting transport phenomena in more complex situations involving realistic 2D and 3D porous media [26–35].

### 3 Unified Algorithm

The YLM is applied to 2D or 3D segmented images; the algorithm described works in both cases without any adaptation. Nonetheless, to be coherent with the images used in the paper, we will use expressions related to the 2D case, such as “pixel” and “circle” rather than “voxel” and “sphere”.

Operations over images commonly require iterated loops over all its pixels. It occurs, for example, when determining the image regions where a circle can be inscribed without overlapping solid pixels, as illustrated in Fig. 2. A first approach is “to move” the circle over the whole image checking whether or not it overlaps solid pixels. Unfortunately, this leads to making operations of the order of  $\mathcal{O}(n^2)$  where  $n$  is the number of pixels in the image. It is something that is computationally unfeasible if it is applied to three-dimensional digital porous media. Additionally, the YLM requires these regions to be found for different circle radii (each radius is associated with a  $P_c$  value by Eq. (1)), so it is essential that the algorithm does not demand all the computations to be remade for each new value. Thus, in order to obtain an efficient YLM algorithm, this question must be carefully addressed.

To the best of the author’s knowledge, there is not any work describing in detail how to implement the YLM efficiently. The solution is to use Mathematical Morphology (MM) algorithms [36] since they allow discovering the region occupied by a predetermined circle, with a very low computational cost operation called *opening* (a more detailed discussion of MM is addressed in Appendix 1). This operation is performed with the aid of the Euclidian Distance Transform (*EDT*), which only needs to be executed once for an image. The EDT can be computed using a very efficient and parallel algorithm proposed by Saito and Toriwaki [37], and the result is a map showing the distance of each pore pixel to the closest solid pixel. Then, when these regions are found, another algorithm is used to discover the regions connected to the source of the invading fluid.

Although improvements regarding drainage simulations were mentioned in previous sections, there are some significant issues that we have not yet addressed. Among them are (i) the compressible behavior of the displaced fluid, (ii) the use of these existing improvements in imbibition simulations, and (iii) the treatment of isolated bubbles of the invading fluid. All of these issues often play a significant role in practical problems.

Previous works [13, 14] devoted some attention to these questions. However, when trying to adapt the method to some selected cases, the authors created countless nomenclatures and notations, which added significant complexity to the algorithm. As described in Sect. 1, these are limiting factors for the wider adoption of the YLM. In this section, we develop a unified algorithm that combines these different solutions in a simpler approach.

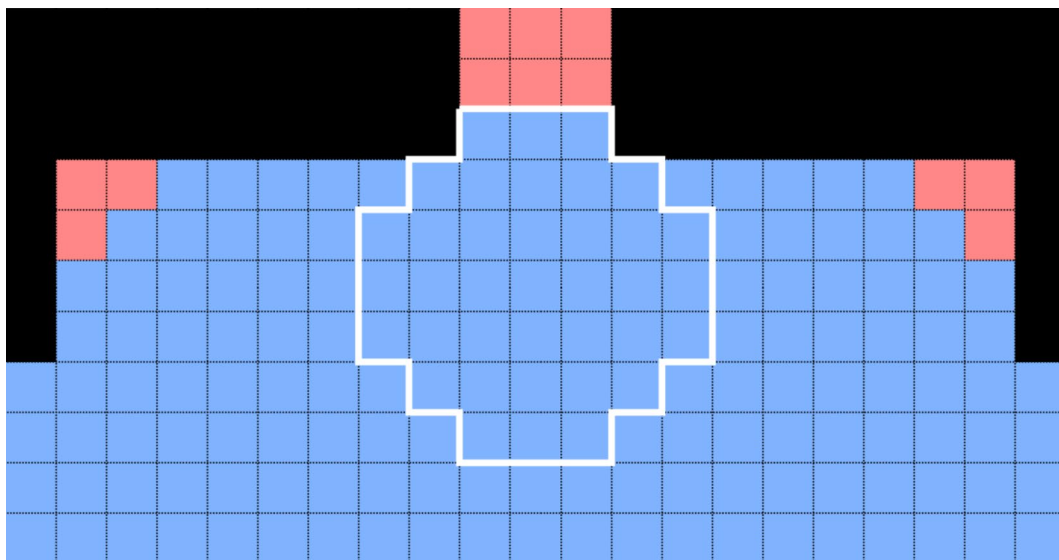


**Fig. 2** Determination of the pixels inside the porous region which can be occupied by a circle of 7 pixels in diameter (region delimited by the white line). The black pixels represent the solid region while the red pixels are the ones that could not be occupied by the circle

### 3.1 Benchmark Geometry

We adopted the benchmark geometry of Mohammadmoradi and Kantzas [7]. Our benchmark is shown in Fig. 3. We have restricted its application to porous media with a simplified 2D geometry to test and exemplify the algorithm's performance in several situations found in, for instance, water/oil-filled rocks: ganglia, dead-end pores, isolated pores, and channels with different shapes and sizes. However, we emphasize the YLM is applied to 2D and 3D cases without any modifications. The wetting (W) and non-wetting (N) fluids are represented by red and blue colors, respectively. The top figure represents the initial state for the drainage, and the bottom figure is the one for the imbibition. In both cases, the inlet is positioned on the left side and the outlet on the right side of the medium. Thus, the dark blue and dark red squares are the source or sink of each fluid, depending on the case.

A semi-permeable membrane was added in different locations in each case. In the drainage process, this membrane is positioned just before the outlet to ensure that the maximum number of pores will be invaded before the fluid finally percolates. For the imbibition process, the membrane is located after the inlet to prevent the invading fluid from filling the whole geometry in a single pressure step.

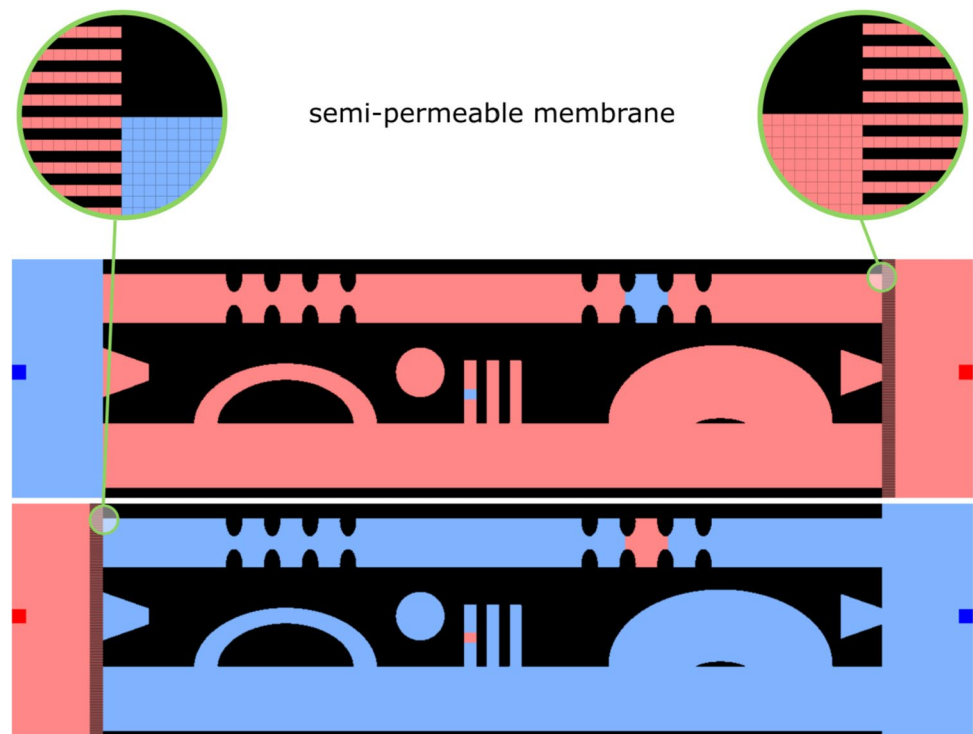
Figure 4a, b show equilibrium states for drainage and imbibition, respectively, for a  $0^\circ$ -contact angle. The case for a  $45^\circ$ -contact angle is shown in Fig. 4c, d. Each case is represented by a two-letter code. The first relates to the wettability of the invading fluid: non-wetting (N) or wetting (W). The second one indicates

if the displaced fluid is incompressible (I) or compressible (C). Thus, the four cases of interest are expressed as NC, NI, WI, and WC. During drainage, the  $P_c$  increases up to the point that the capillary diameter reaches a pixel length (Eq. (1)). In the imbibition the opposite occurs, i.e., initially, the  $P_c$  is high, and as the pressure decreases, the wetting fluid starts to occupy the available channels. For all four cases, the algorithm provided physically consistent results. Each row in the figures states a specific value of the  $P_c$ , and they resulted from a sequence of operations applied over the regions of interest of the benchmark images (Fig. 3). These operations are described in the next section.

### 3.2 Algorithm's Description

The first step in building this framework is to identify the minimal set of regions of interest over which the operations will be performed. Since each of these regions is represented computationally by a matrix, the use of too many of them results in a high computational cost, and it is time-consuming. While Hazlett [12] defined these regions vaguely, Magnani [13] and Magnani et al. [14] used a non-necessary large number of regions. Hilpert and Miler [4] presented a clear definition while providing simple operators to manipulate these regions based on the Mathematical Morphology formalism. Thus, in this present work, we keep their definitions, where the current state is defined by three regions: the invading fluid, the displaced fluid, and the solid. Additionally, some pixels must be labeled as the source and sink of the invading and displaceable fluids.

**Fig. 3** The benchmark geometry used to analyze and demonstrate the unified algorithm. The top and bottom figures represent the initial fluids distribution for drainage and imbibition, respectively. The wetting and non-wetting fluids are represented, respectively, by red and blue colors. In both cases, the inlet is positioned on the left side and the outlet on the right side of the medium. Thus, the dark blue and dark red squares are the source or sink of each fluid, depending on the case



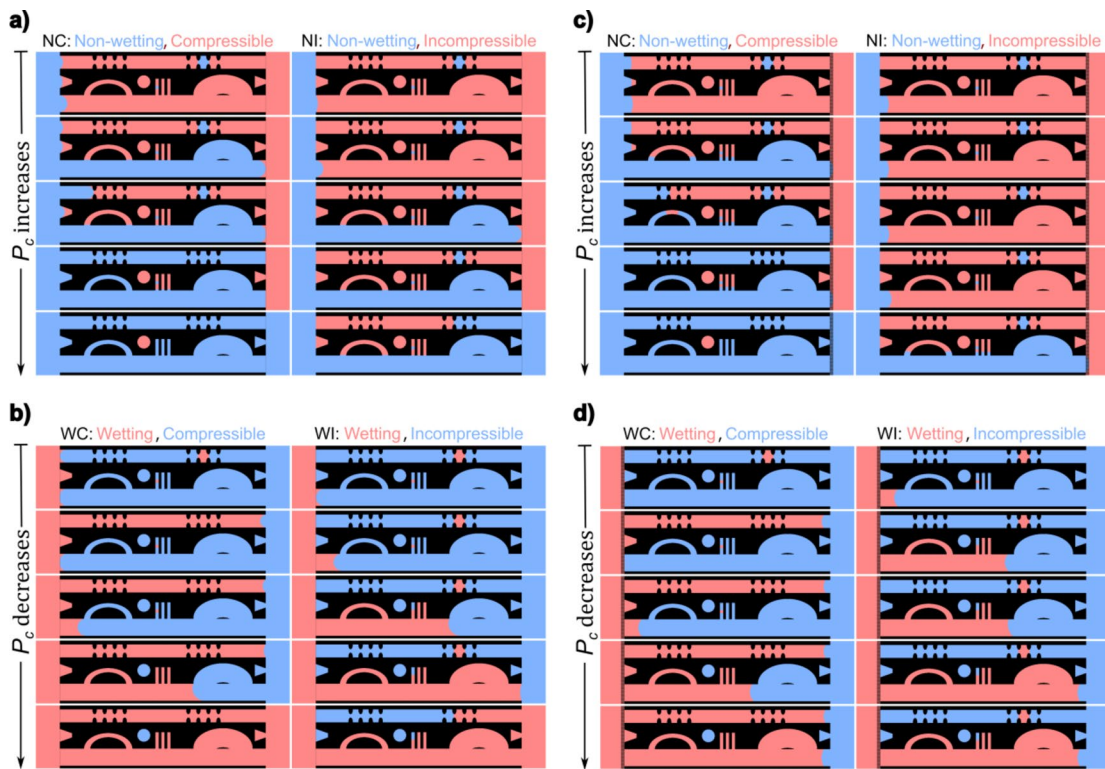


**Fig. 4** Selected equilibrium states for the drainage (a and c) or imbibition (b and d) using the unified YLM algorithm in the benchmark geometries with a contact angle of 0° (a and b) or 45° (c and d). Each case is represented by a two-letter code. The first relates to the wet-

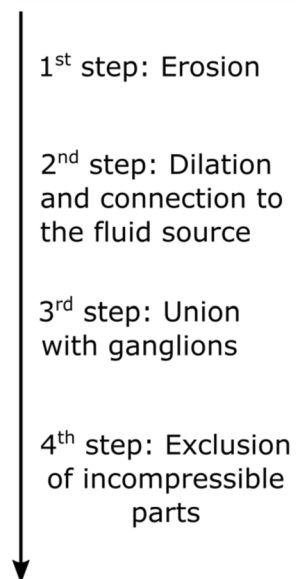
tability of the invading fluid: non-wetting (N) or wetting (W). The second one indicates if the displaced fluid is incompressible (I) or compressible (C)

Figure 5 shows a schematic picture of the YLM algorithm. We use image analysis notation based on set operations. The sequence and number of proposed operations were designed to allow a unified algorithm for the four cases of interest (NC, NI, WI, and WC). Each column of the figure represents each

of these cases. For a better organization, the operations are grouped into four steps, with the last step being performed solely for the two incompressible cases (NI and WI).

Common to all cases, the first step (Fig. 5) erodes the porous region ( $P$ ) using a circle as a structuring element ( $D'$ ),

**Fig. 5** The Algorithm structure is shown in four steps. Set operations represent the algorithm structure for each of the four cases. The symbols are: porous region ( $P$ ), structuring element ( $D'$ ), 1st step set ( $A_i$ ), 2nd step operations ( $N_i^{(k)}$  or  $W_i^{(k)}$ , it depends on the case), filtering process at the invading fluid source ( $F_{Iv}$ ), distribution of the invading fluid at the previous pressure step ( $I_{i-1}$ ), 3rd step set ( $B_i$ ), 4th step operations ( $C_i^{(k)}$ ), filtering process at the displaced fluid sink ( $F_{Ov}$ ), and distribution of the displaced fluid at the previous pressure step ( $O_{i-1}$ )



NC	NI	WI	WC
$A_i \equiv P \ominus D'$			
$N_i^{(0)} \equiv A_i \cup I_{i-1}$ $N_i^{(1)} \equiv F_{Iv} \left( N_i^{(0)} \right)$ $N_i^{(2)} \equiv N_i^{(1)} \cap A_i$ $N_i^{(3)} \equiv N_i^{(2)} \oplus D$		$W_i^{(0)} \equiv A_i \oplus D$ $W_i^{(1)} \equiv P \setminus W_i^{(0)}$ $W_i^{(2)} \equiv W_i^{(1)} \cup I_{i-1}$ $W_i^{(3)} \equiv F_{Iv} \left( W_i^{(2)} \right)$	
$B_i \equiv N_i^{(3)} \cup I_{i-1}$		$B_i \equiv W_i^{(3)} \cup I_{i-1}$	
$C_i^{(0)} \equiv O_{i-1}$ $C_i^{(1)} \equiv F_{Ov} \left( C_i^{(0)} \right)$ $C_i^{(2)} \equiv B_i \setminus C_i^{(1)}$ $C_i^{(3)} \equiv F_{Iv} \left( C_i^{(2)} \right)$ $C_i^{(4)} \equiv C_i^{(3)} \cup I_{i-1}$			

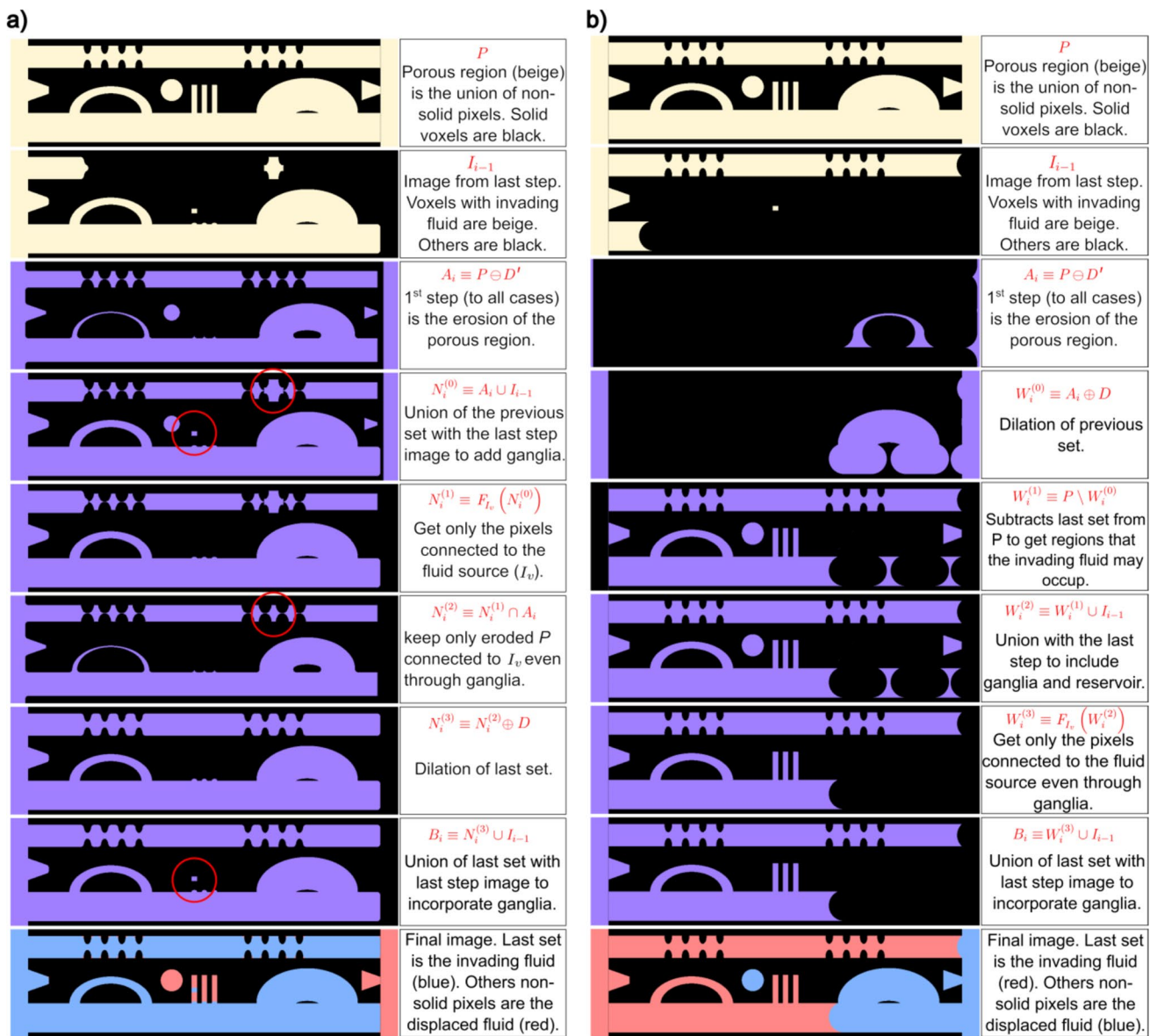


**Fig. 6** Image analysis operations to determine the distribution of fluids in one pressure step. **a** Drainage: the invading fluid is non-wetting and the displaced fluid is fully compressible (NC). **b** Imbibition: the invading fluid is wetting, and the displaced fluid is fully compressible (WC). The fluid source  $I_v$  is at the extreme left and the fluid sink  $O_v$

at the extreme right. The beige pixels represent the input data of the algorithm: porous region and initial (or previous pressure step) distribution of the invading fluid. The purple pixels indicate the operations performed to find the final image that represents the obtained result for the one-step drainage or imbibition

resulting in the  $A_i$  set. The second one consists of a group of four operations ( $N_i^{(k)}$  for NC and NI;  $W_i^{(k)}$  for WC and WI) that expands the previous region excluding parts not connected to the input fluid source. The symbol  $F_{I_v}$  denotes the operation or filtering process that guarantees that only the sections connected to the invading fluid source ( $I_v$ ) should remain, and  $I_{i-1}$  indicates the distribution of the invading fluid at the previous pressure step. The operations order depends on the type of fluid, as shown in Fig. 5.

After identifying the regions occupied by the invading fluid, associated with a  $P_c$ , the regions originally disconnected (ganglia) are included in the third step, indicated by  $B_i$  (Fig. 5). If the displacement fluid is fully compressible (NC/WC), this is the last stage for the current  $P_c$ . However, if the displaced fluid is incompressible (NI and WI), it is still necessary to exclude its parts that are not connected to the sink. It happens as the fluid has no place to flow to, and it cannot be compressed; then, this portion of the fluid

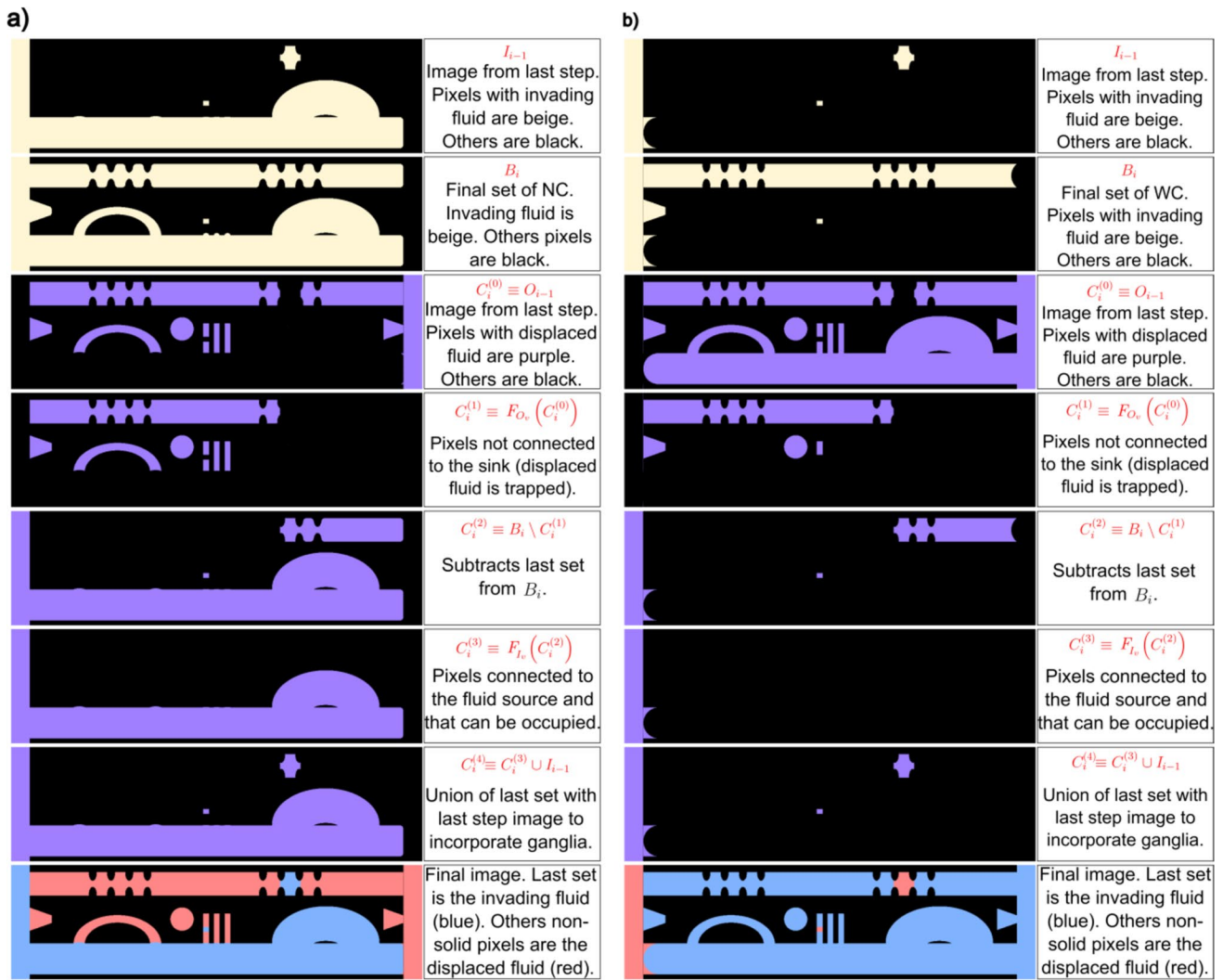


**Fig. 7** Image analysis operations to determine the distribution of fluids in one pressure step. **a** Drainage: the invading fluid is non-wetting and the displaced fluid is fully incompressible (NI). **b** Imbibition: the invading fluid is wetting, and the displaced fluid is fully incompressible (WI). The fluid source  $I_v$  is at the extreme left and the fluid sink

$O_v$  at the extreme right. The beige pixels represent the input data of the algorithm: porous region and initial (or previous pressure step) distribution of the invading fluid. The purple pixels indicate the operations performed to find the final image that represents the obtained result for the one-step drainage or imbibition

remains trapped in its position in the structure. The fourth step (Fig. 5) operation is indicated by the  $C_i^{(k)}$ . In a similar way to  $F_{I_v}$  and  $I_{i-1}$ ,  $F_{O_v}$ , is the filtering process that guarantees that only the sections connected to the displaced fluid sink ( $O_v$ ) should remain, and  $O_{i-1}$  indicates the distribution of the displaced fluid at the previous pressure step.

The results of each step in Fig. 5 performed by the YLM algorithm are exemplified and commented in Figs. 6 (NC and WC cases) and 7 (NI and WI cases) for one of the pressure steps. As for the input data, no special requirement was imposed on the initial fluids distribution or by the geometry, the algorithm is rather general.

The capillary curve is then obtained by applying the following equation with different radii for the circle, whose values are given by the  $P_c$  using the Young–Laplace Equation (Eq. (1)).

$$s(r) = \frac{\sum \{ [F_{I_v}(P \ominus D')] \oplus D \}}{\sum P} \tag{2}$$

where  $s(r)$  is the saturation of the invading fluid for a circle radius ( $r$ , and  $D' \equiv D'(r)$ ), and the summation symbol represents the operation of counting the pixels of each region, and the operator  $F_{I_v}$ , denotes the process of filtering the pixels connected with the invading fluid source.



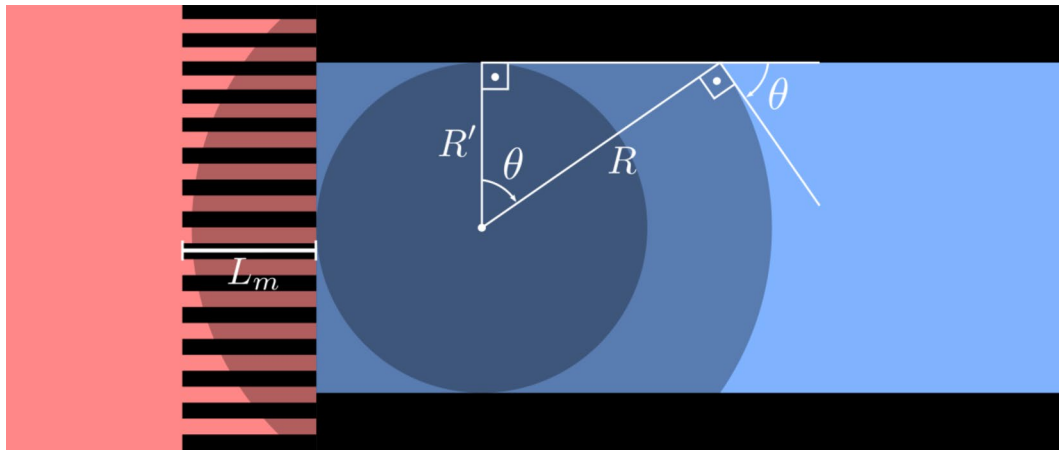


**Fig. 8** Attempt to use the generalization by Schulz et al. [5] to simulate imbibition with a different wettability angle. Erosion for a circle radius and subsequent dilation by a circle of a larger radius is indicated in the same image

### 4 Imbibition Case

As discussed earlier, the correction proposed by Hilpert and Miller [4] and the generalization proposed by Schulz et al. [5] to YLM were not applied to the imbibition case in other works. In this section, we show that there was no need to use Hilpert’s correction for imbibition and that the Schulz generalization can be applied to it, only if an appropriate membrane is used.

In drainage, larger channels drain first unless there is a narrow channel in the pathway to restrict them. The restriction is due to the higher  $P_c$  required for draining these narrow channels. It is called the *ink bottle effect*. The approach proposed by Hilpert and Miller [4] is applied to correct an overestimated saturation due to *ink bottle* geometries inside the porous space after the *opening* process (see Fig. 13 in Appendix 2). However, the same effect cannot happen on imbibition because the smaller channels fill first. Therefore, Hilpert’s correction is unnecessary for imbibition.

The generalization of Schulz et al. [5] to other contact angles can be very useful in imbibition since wettability is an important factor. Nevertheless, as far as we know, it has never yet been described. Figure 8 shows that according to the Schulz process the *dilation* with  $R\cos\theta$  results in a displaced fluid that moves backward, preventing the wetting fluid from entering the membrane and, subsequently, in the channel. The solution is straightforward: use an elongated membrane with a length greater than the difference in radii of the two circles,

$$L_m > R - R' = R' \left( \frac{1}{\cos\theta} - 1 \right) \tag{3}$$

where  $L_m$  is the membrane length,  $R'$  is the half channel width, and  $\theta$  is the contact angle as indicated in Fig. 8. Some selected simulation steps are shown in Fig. 4a, c for contact angles of  $0^\circ$  and  $45^\circ$ , respectively.

### 5 Conclusion

In this work, we presented an algorithm to simulate capillary-driven two-phase fluid flow in porous media by combining several previous works into a single unified framework. Following Hazlett [12], Magnani [13], and Magnani et al. [14], the algorithm uses the Mathematical Morphology formalism. We also incorporated improvements from Hilpert and Miller [4] and Schulz et al. [5]. In addition to the unified structure, we offer, for the first time in the literature, a complete and detailed description of the YLM algorithm and show how to apply it in the imbibition case.

This generalized framework allows the simulation of both drainage and imbibition problems with the displaced fluid being either fully compressible or incompressible. The unified algorithm is also capable of handling any geometry or initial fluid distributions. So, one possibility of application for this unified algorithm is predicting the hysteretic characteristic of the soil retention curve by drying and wetting cycles. However, it is not limited to this application.

Finally, we offer an open-source C++ code for it, something that will help the YLM to gain even more space in different applications involving transport phenomena in digital porous media.

## 6 Computer Code Availability

The Young–Laplace Method unified algorithm is available as a C++ source code, accompanied by Python 3+ example scripts. The source code is licensed under the GPL-3.0 License. The source code and examples can be downloaded from the data repository [38].

### Appendix 1. Mathematical Morphology Applied to YLM

Figure 9 illustrates how the region occupied by the invading fluid is found using Mathematical Morphology (MM) operations. In the YLM, it is considered that the image is exclusively formed by the union between the solid and pore ( $P$ ) related pixels and that the MM operations will not expand the image beyond its original dimensions.

In MM, the *opening operation* ( $\circ$ ) is defined using the combination of two fundamental operations: *erosion* and *dilation*. In the *erosion operation*, denoted by  $\ominus$ , a structuring element with a disk shape  $D$  is applied over the region  $P$  (Fig. 9a), resulting in region  $E = P \ominus D$ , as shown in Fig. 9b. Region  $E$  comprises all the points in  $P$ , where the structuring element can be centered without overlapping the solid region. Notice that although no segment can overlap over the solid region, it is allowed for part of the structuring element to be outside of the boundary image.

Figure 9c exemplifies the *dilation operation* of  $E$  by a structuring element  $D$  (denoted by  $E \oplus D$ ), resulting in region  $O$  with all the points intersected by the disk  $D$  as its center moves around the  $E$  region. It is important to notice that the result includes only points originally belonging to  $P$ ; otherwise, the final image would be expanded.

Lastly, Fig. 9c is also the region  $O$  obtained directly as a result of the *opening operation* of  $P$  by the structuring element  $D$  ( $O = P \circ D$ ), which comprises all the points of  $D$ , as this element moves around  $P$  without extending over the solid region. As the case shown in Fig. 9b, the structuring element is allowed to lay over regions outside the image. Moreover, as in Fig. 9c, the resulting region  $O$  contains only points belonging initially to  $P$ . Figure 9d shows the final results after relabeling the porous region.

As one can realize from Fig. 9, the *erosion* of  $P$  by  $D$  followed by the *dilation* by  $D$  is identical to the *opening* of  $P$  by  $D$ , i.e.,

$$O = P \circ D = E \oplus D = (P \ominus D) \oplus D \quad (4)$$

Actually, it is possible to prove that it represents a general result, which is of great practical importance because it allows performing the *opening* operation using the combination of *dilation* and *erosion* operations. Furthermore, *dilation* can be obtained by applying *erosion* to the negative of an image. The negative is retrieved by swapping the image foreground and background, which in our case are porous and solid regions, respectively. Denoting the negative by an overbar, one can show that

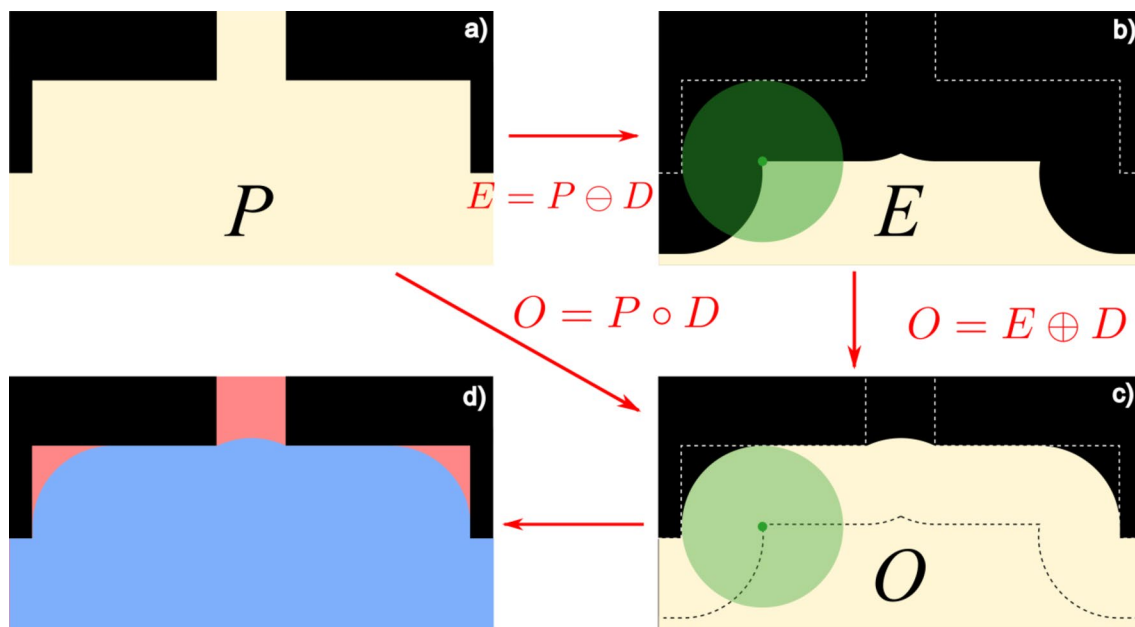


**Fig. 9** Examples of the fundamental MM operations. **a** The porous region  $P$  is shown in beige. **b** and **c** The beige region represents the set of points resulting from the operations of erosion and dilation, respectively. **d** The final result

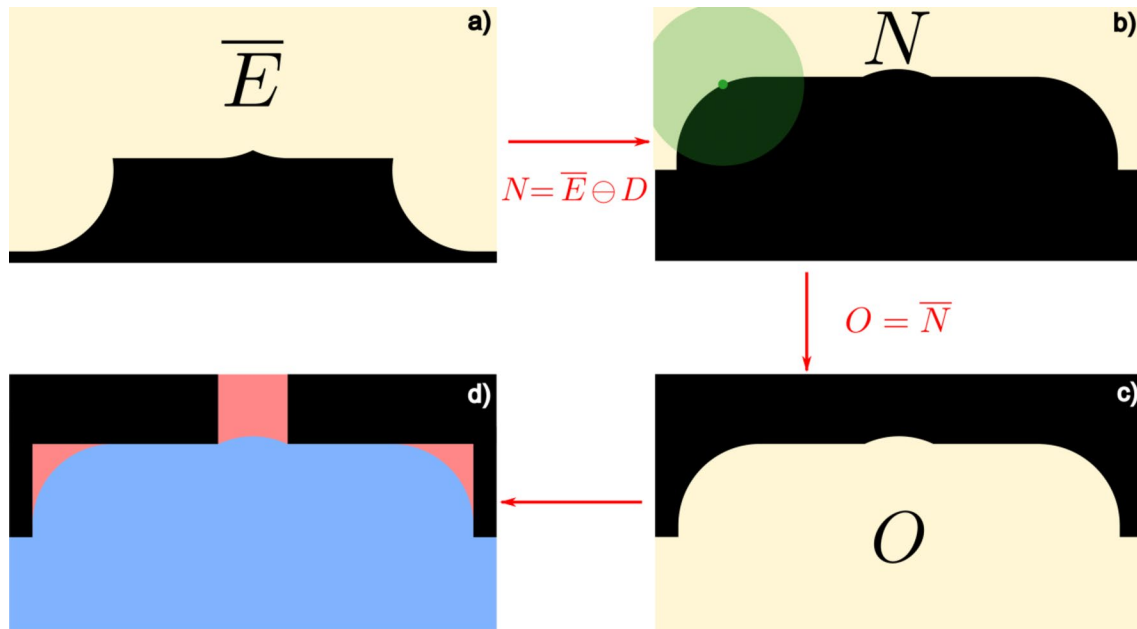


**Fig. 10** The opening operation of  $P$  is performed by two erosion operations. This is possible because the negative of the dilation is equal to the erosion of the negative. **a** Results from the negative of

the  $E$  region in Fig. 9b. **b** and **c** The beige region represents the set of points resulting from the operations of erosion and the negative of the  $N$  region, respectively. **d** The final result

$$E \oplus D = \overline{(\overline{E} \ominus D)} \tag{5}$$

The right-hand side operation is shown in Fig. 10a–d, which gives the same result already displayed in Fig. 9, which depicts the operation of the left-hand side. Using Eq. (5), the opening operation in Eq. (4) is written solely in terms of erosions

$$O = \overline{(\overline{E} \ominus D)} = \overline{(\overline{(P \ominus D)} \ominus D)} \tag{6}$$

As previously mentioned, to obtain an efficient algorithm, the erosion operations must be performed with the aid of the Euclidian Distance Transform (EDT). The result of the EDT is a map with the distance of each pore pixel to the closest solid pixel, and it can be computed using a very efficient and parallel algorithm proposed by Saito and Toriwaki [37].

If the structuring element is a circle of radius  $R$ , then the erosion operation is given by the set of pixels whose distance to the solid is larger than  $R$  or, equivalently,  $EDT_{ij}^2 > R^2$  where  $EDT_{ij}^2$  indicates the squared distance of the pixel located at the image position  $ij$  to the closest solid pixel [39]. Using the squared distance is advantageous since it allows for the computation to be handled solely by integers. Figure 11 depicts how the EDT can be used to compute the opening operation of the porous region by a circle. The

procedure starts from the EDT result, shown in Fig. 11a. As explained, the values are the squared distance to the background (solid). By taking the negative of this result, i.e., setting it as background (Fig. 11b), the EDT is once again applied from which a new erosion is performed. The negative result of this last operation (Fig. 11c) gives the opening of the porous region by the circle (Fig. 11d).

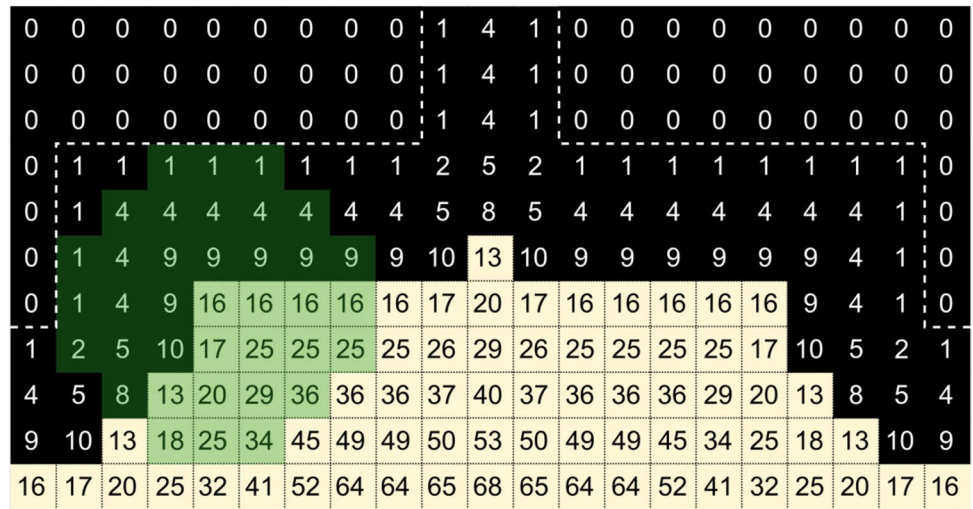
Figure 12 illustrates the bottom-up drainage through a narrow channel. The non-wetting fluid source is represented by the dark blue square (Fig. 12a). By the opening operation, and consequently, by the Young–Laplace equation, the upper region could be occupied by the non-wetting fluid; however, the circle cannot cross the constriction for this radius (Fig. 12b). From the morphological standpoint, this question is addressed by discarding the upper region since it is not connected to the source.

The next step is the identification of the connection between the regions can be performed by using the algorithm of He et al. [40]. This technique assigns a label to each unconnected group of pixels, allowing us to ignore the pixels with labels different from that of the sources (Fig. 12c). This methodology already considers the possibility of multiple sources.

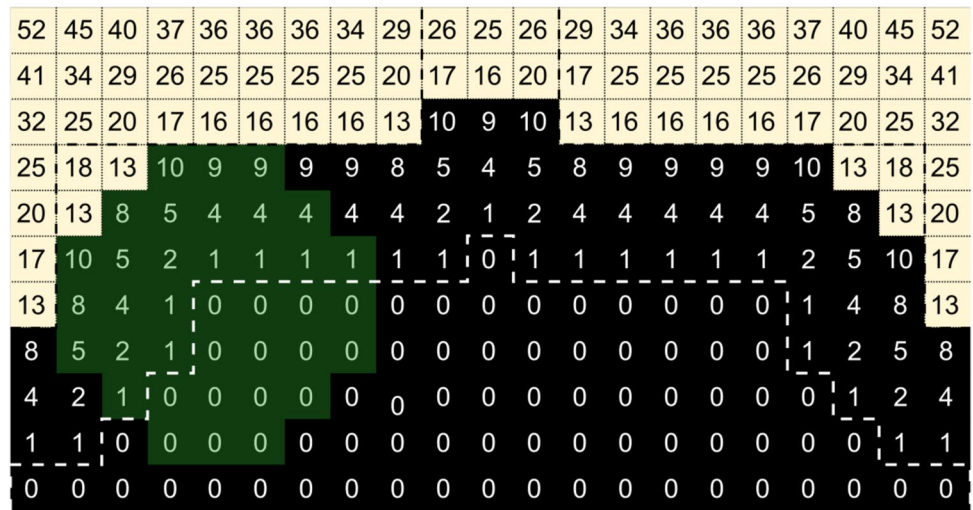
By using the MM notation discussed above, the YLM can be expressed as [4]:

$$s(r) = \frac{\sum F_v(P \circ D)}{\sum P} \tag{7}$$

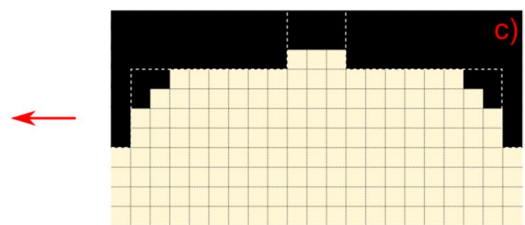
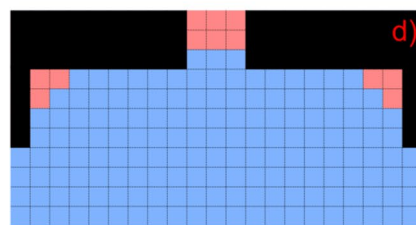
**Fig. 11** Opening operation of the porous region by a circle of 7 pixels in diameter (i.e.,  $R^2 = 3.5^2 = 12.25$ ) using the EDT (see Fig. 2). **a** EDT values used to erode the porous region. **b** EDT values used to erode the negative image of **a**. **c** The negative image of **b** is equivalent to the opening operation of the porous region directly. **d** Final image after opening operation of the porous region by a circle of 7 pixels in diameter



a)



b)



c)

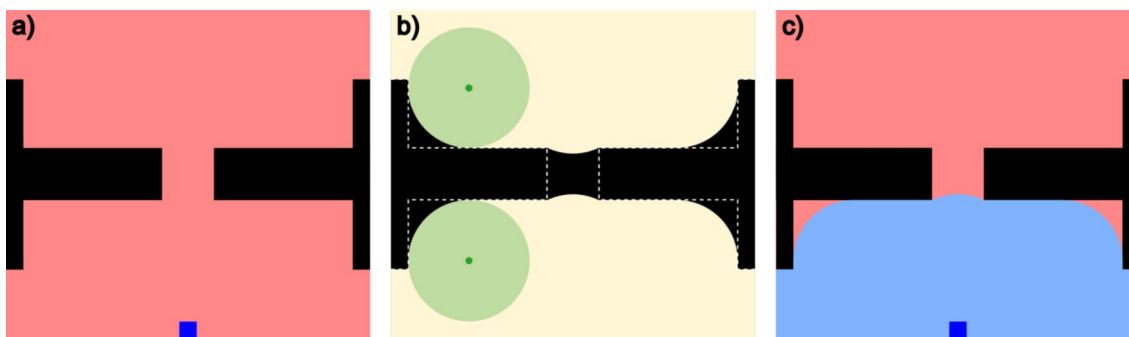


**Fig. 12** **a** A bottom-up drainage through a narrow channel with the wetting fluid in red, and the non-wetting fluid source represented by the dark blue square. **b** The opening operation identifies two regions (beige color) that could be occupied by **c** the invading non-wetting

fluid (light blue), but the upper region is not connected to the fluid source (dark blue pixel), and hence cannot be filled in the current pressure step

where  $s(r)$  is the saturation of the invading fluid for a given circle radius ( $r$ , and  $D \equiv D(r)$ ), and the summation symbol represents the operation of counting the pixels of each region. As for the operator  $F_v$ , it denotes the process of filtering the pixels connected with the invading fluid source.

As described in Sect. 2, imbibition can be obtained in a similar way to the drainage processes. But actually, some implementation details distinguish these two processes. These differences were noticed by the earlier authors of the method [12–14], and they were discussed in Sect. 3.

### Appendix 2. Main Improvements for Drainage Simulation with the YLM

Since the majority of the applications of the YLM are limited to drainage simulations, this process received greater attention from researchers over the years compared to imbibition. Consequently, important improvements were proposed in the literature for the drainage process, and here, we describe two significant changes to the original procedure summarized by Eq. (7).

Hilpert and Miller [4] identified an error in Eq. (7) which led to an overestimation of the saturation value in some situations. As displayed in Fig. 13a, for a drainage process of the wetting fluid (red) from the bottom to the top in a selected geometry with two large pore regions separated by a short channel (like an *ink bottle* geometry), the *opening* operation results in the two regions being connected (Fig. 13c). Nevertheless, during a real invasion, the non-wetting fluid (blue) would not reach the upper section for the value of pressure related to the circle radius indicated in Fig. 13b, since it cannot cross the channel. This would only be possible if the entire circle could cross the channel.

To avoid this error, Hilpert and Miller [4] proposed a simple correction (Fig. 13d) that consists of identifying the regions connected to the fluid source between the *erosion* (Fig. 13b) and the *dilation* (Fig. 13f) processes instead of after the *dilation* (Fig. 13e). Figure 13g, h shows the difference between the original YLM drainage and Hilpert’s correction YLM drainage, respectively. Considering this correction, Eq. (7) is replaced by

$$s(r) = \frac{\sum \{ [F_v(P \ominus D)] \oplus D \}}{\sum P} \tag{8}$$

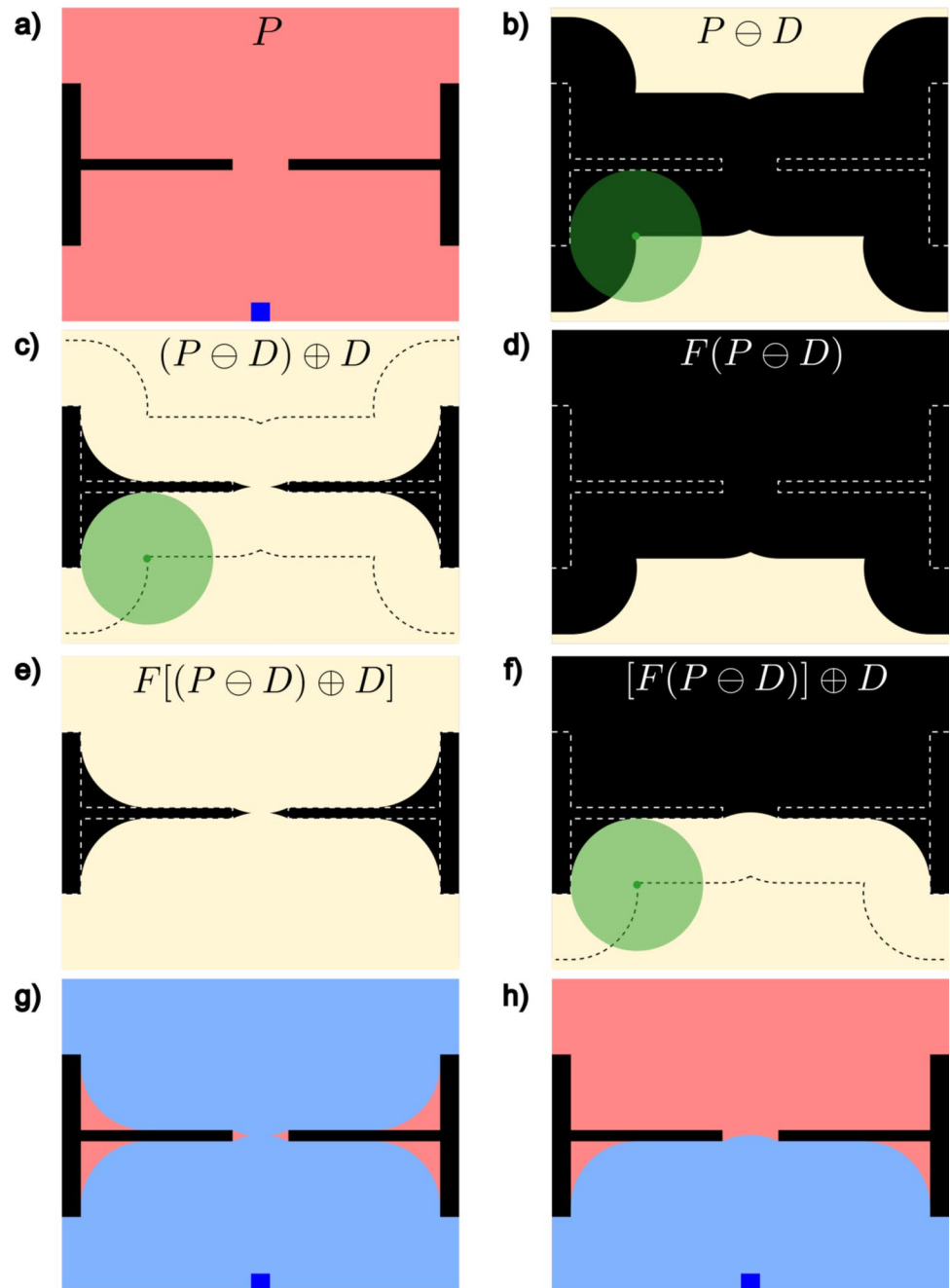
The drainage process described by Eq. (8) is limited to the simulation of the invasion of a fully non-wetting fluid, or equivalently, the value for the contact angle in Fig. 1a is always zero. Schulz et al. [5] presented a small modification to this algorithm, allowing different values to be set. The concept used by the authors is depicted in Fig. 14. It shows that if a circle with a different radius is used ( $R'$  for *erosion* and  $R$  for *dilation*); then, a final interface with a radius of curvature  $R'$  and contact angle  $\theta$ , given by

$$R' = R \cos\theta \tag{9}$$

is achieved. Including this improvement, Eq. (8) is modified to Eq. (2) in which the structuring element  $D'$  is associated with a circle with a radius  $R'$ . Even though this generalization enables more realistic applications of the YLM, a fact that it is not yet widely known by the research community, as recent works still point out the inability to change the contact angle [10, 41].

One main advantage of this approach is concerning to its implementation easiness. Since just the radius of the *erosion* needs to be modified, it is easily incorporated into an existing YLM code. Moreover, as the *erosion* is computed pixel by pixel using the EDT result, a case of mixed

**Fig. 13** **a** A drainage process of the wetting fluid (red) from the bottom to the top in a selected geometry with two large pore regions separated by a short channel. Common to both cases, the erosion operations are performed in **b**, **c**, **e**, and **g**. The original YLM drainage algorithm as proposed by Hazlett [12] and also by Magnani [13] and Magnani et al. [14], **d**, **f**, and **h**. The correction of Hilpert and Miller [4]. The non-wetting invading fluid (blue) source is represented by a dark blue square



wettability could be readily performed by assigning an individual contact angle to each pixel [5].

On the other hand, since the porous media surface is, in general, curved, the contact angle will depend on this curvature. Also, if the larger circle used in the *dilation* extends beyond the wall to a near pore, this region can be incorrectly assigned as occupied by the invading fluid. Although, for it to happen, this region must also have a connection with the fluid source. This situation is shown

in Fig. 14, where the circle with a radius  $R'$  extends to a bottom channel.

As mentioned by the authors, in petrophysics applications, these two drawbacks do not present a serious problem if  $\theta \lesssim 40^\circ$  as the rock samples generally have low porosity and a large number of small pores.

As shown in Sect. 4, an appropriate membrane makes Schulz's proposed modification suitable even for imbibition.

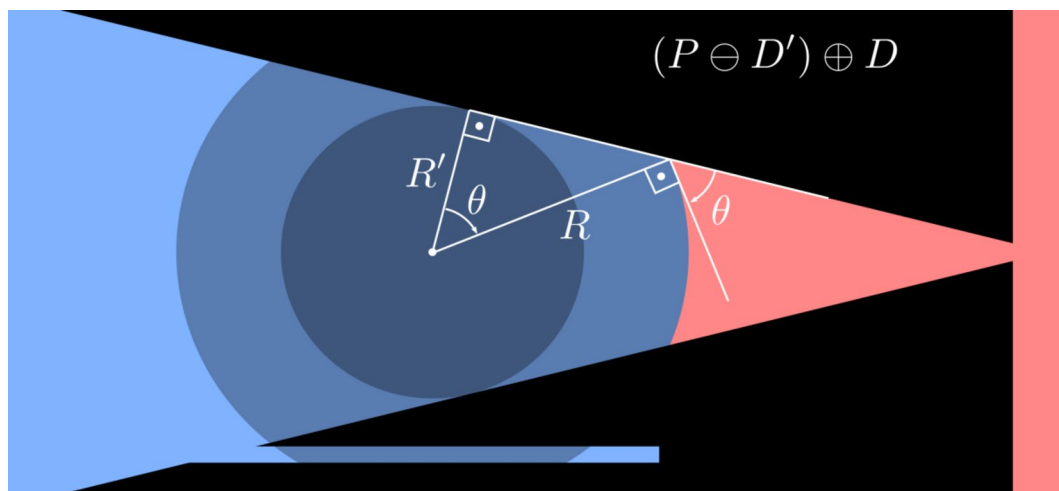


**Fig. 14** The sequence of MM operations proposed by Schulz et al. [5] to enable drainage simulations with different contact angles. The disks  $D'$  and  $D$  are associated with  $R'$  for erosion and  $R$  for dilation, respectively

**Acknowledgements** The authors are grateful to the Brazilian Petroleum Company (Petrobras) for the financial support.

**Author Contributions** A.M.Z.: conceptualization, methodology, software, and writing—original draft; M.A.C.: writing—review and editing; F.G.W.: validation, resources, writing—review and editing, and funding acquisition; D.N.S.: resources, writing—review and editing, and funding acquisition; R.S.: software, resources, and funding acquisition; L.O.E.S.: conceptualization, writing—review and editing; T.R.F., L.F.P., and F.A.M.C: writing—review and editing.

**Funding** Fabiano G. Wolf, Diogo Siebert, and Rodrigo Surmas report financial support provided by the Brazilian Petroleum Company (Petrobras) (project numbers 4600386529 and 2015/00388–4).

**Availability of Data and Material** Not applicable.

**Code Availability** An open-source C++ code for the proposed unified algorithm is available at: <https://github.com/alexandrezabot/ylm>.

## Declarations

**Conflict of Interest** The authors declare no competing interests.

## References

- V.P. Schulz, J. Becker, A. Wiegmann, P.P. Mukherjee, C.-Y. Wang, *J. Electrochem. Soc.* **154**, B419 (2007)
- H.-J. Vogel, J. Tölke, V.P. Schulz, M. Krafczyk, K. Roth, *Vadose Zo. J.* **4**, 380 (2005)
- D. Adalsteinsson, M. Hilpert, *Transp. Porous Media* **65**, 337 (2006)
- M. Hilpert, C.T. Miller, *Adv. Water Resour.* **24**, 243 (2001)
- V.P. Schulz, E.A. Wargo, E.C. Kumbur, *Transp. Porous Media* **107**, 13 (2015)
- I. Shikhov, C.H. Arns, *Transp. Porous Media* **107**, 623 (2015)
- P. Mohammadmoradi, A. Kantzas, *Adv. Water Resour.* **94**, 200 (2016)
- Y. Mu, R. Sungkorn, J. Toelke, *Adv. Water Resour.* **95**, 16 (2016)
- S. Berg, M. Rücker, H. Ott, A. Georgiadis, H. van der Linde, F. Enzmann, M. Kersten, R.T. Armstrong, S. de With, J. Becker, A. Wiegmann, *Adv. Water Resour.* **90**, 24 (2016)
- P. Mostaghimi, R.T. Armstrong, A. Gerami, Y. Hu, Y. Jing, F. Kamali, M. Liu, Z. Liu, X. Lu, H.L. Ramandi, A. Zamani, Y. Zhang, *J. Nat. Gas Sci. Eng.* **39**, 143 (2017)
- S.N. Apourvari, C.H. Arns, *Adv. Water Resour.* **95**, 161 (2016)
- R.D. Hazlett, *Transp. Porous Media* **20**, 21 (1995)
- F.S. Magnani, *Determinação Das Configurações de Equilíbrio Em Meios Porosos Indeformáveis*, Universidade Federal De Santa Catarina, 1996
- F.S. Magnani, P.C. Philippi, Z.R. Liang, C.P. Fernandes, *Int. J. Multiph. Flow* **26**, 99 (2000)
- P. Mohammadmoradi, A. Kantzas, in *Day 3 Tue, April 25, 2017 (SPE, 2017)*
- S.P. Mohammadmoradi, *Pore morphological multi-phase digital rock physics models*, UNIVERSITY OF CALGARY, 2016
- D. Tiab, E.C. Donaldson, *Petrophysics: Theory and Practice of Measuring Reservoir Rock and Fluid Transport Properties*, 4th edn. (Gulf Professional Publishing, 2015)
- M.A. Celia, P.C. Reeves, L.A. Ferrand, *Rev. Geophys.* **33**, 1049 (1995)
- J.Y. Zuo, X. Guo, Y. Liu, S. Pan, J. Canas, O.C. Mullins, *Energy Fuels* **32**, 4705 (2018)
- A. Mehmani, M. Prodanović, *Adv. Water Resour.* **63**, 104 (2014)
- T. Zhang, S. Sun, *Energies* **14**, 7724 (2021)
- H. Huang, D.T. Thorne, M.G. Schaap, M.C. Sukop, *Phys. Rev. E* **76**, 066701 (2007)
- X. Shan, H. Chen, *Phys. Rev. E* **47**, 1815 (1993)
- X. Shan, G. Doolen, *J. Stat. Phys.* **81**, 379 (1995)
- F.G. Wolf, D.N. Siebert, R. Surmas, *Phys. Fluids* **32**, 052008 (2020)
- J. Zhang, *Microfluid. Nanofluidics* **10**, 1 (2011)
- S.A. Galindo-Torres, A. Scheuermann, L. Li, D.M. Pedrosa, D.J. Williams, *Comput. Phys. Commun.* **184**, 1086 (2013)
- C.J. Landry, Z.T. Karpyn, O. Ayala, *Water Resour. Res.* **50**, 3672 (2014)
- I. Zacharoudiou, E.S. Boek, *Adv. Water Resour.* **92**, 43 (2016)
- J. Wang, L. Chen, Q. Kang, S.S. Rahman, *Fuel* **181**, 478 (2016)
- Q. Liu, Y.-L. He, *Phys. A Stat. Mech. Its Appl.* **465**, 742 (2017)

32. Z. Li, S. Galindo-Torres, G. Yan, A. Scheuermann, L. Li, *Adv. Water Resour.* **116**, 153 (2018)
33. Z. Peng, S. Liu, S. Tang, Y. Zhao, Y. Li, *Geofluids* **2018**, 1 (2018)
34. T. Zhang, S. Sun, *Fuel* **246**, 196 (2019)
35. J. Zhao, F. Qin, D. Derome, J. Carmeliet, *J. Hydrol.* **588**, 125080 (2020)
36. P. Soille, *Morphological Image Analysis* (Springer, Berlin Heidelberg, Berlin, Heidelberg, 2004)
37. T. Saito, J.-I. Toriwaki, *Pattern Recognit.* **27**, 1551 (1994)
38. A. Zobot, (2022)
39. C.A. Glasbey, G.W. Horgan, *Image Analysis for the Biological Sciences*, 1st edn. (Wiley, 1995)
40. L.-F. He, Y.-Y. Chao, K. Suzuki, *J. Comput. Sci. Technol.* **28**, 468 (2013)
41. M.A. Camargo, F.A.M. Cássaro, L.F. Pires, *Bull. Eng. Geol. Environ.* **81**, 137 (2022)

**Publisher's Note** Springer Nature remains neutral with regard to jurisdictional claims in published maps and institutional affiliations.

Springer Nature or its licensor (e.g. a society or other partner) holds exclusive rights to this article under a publishing agreement with the author(s) or other rightsholder(s); author self-archiving of the accepted manuscript version of this article is solely governed by the terms of such publishing agreement and applicable law.